Floodplain Land Cover and Flow Hydrodynamic Control of Overbank Sedimentation in Compound Channel Flows

Juez, Carmelo; Schärer, C.; Jenny, H.; Schleiss, A. J.; Franca, M. J.

DOI
10.1029/2019WR024989

Publication date
2019

Document Version
Final published version

Published in
Water Resources Research

Water Resources Research

RESEARCH ARTICLE
10.1029/2019WR024989

Floodplain Land Cover and Flow Hydrodynamic Control of Overbank Sedimentation in Compound Channel Flows

Carmelo Juez[1,2,3], C. Schärer[1], H. Jenny[1], A. J. Schleiss[1], and M. J. Franca[4,5]

[1]École Polytechnique Fédérale de Lausanne (EPFL), Laboratoire de Constructions Hydrauliques (LCH), Lausanne, Switzerland, [2]Universidad Politécnica de Madrid (UPM), ETSIDI, Madrid, Spain, [3]Instituto Pirenaico de Ecologa, Consejo Superior de Investigaciones Cientficas (IPE-CSIC), Zaragoza, Spain, [4]IHE-Delft Institute for Water Education, Water Science and Engineering department, Delft, The Netherlands, [5]Department of Hydraulic Engineering, Delft University of Technology, Delft, The Netherlands

Abstract Overbank sedimentation is predominantly due to fine sediments transported under suspension that become trapped and settle in floodplains when high-flow conditions occur in rivers. In a compound channel, the processes of exchanging water and fine sediments between the main channel and floodplains regulate the geomorphological evolution and are crucial for the maintenance of the ecosystem functions of the floodplains. These hydrodynamic and morphodynamic processes depend on variables such as the flow-depth ratio between the water depth in the main channel and the water depth in the floodplain, the width ratio between the width of the main channel and the width of the floodplain, and the floodplain land cover characterized by the type of roughness. This paper examines, by means of laboratory experiments, how these variables are interlinked and how the deposition of sediments in the compound channel is jointly determined by them. The combination of these compound channel characteristics modulates the production of vertically axised large turbulent vortical structures in the mixing interface. Such vortical structures determine the water mass exchange between the main channel and the floodplain, conditioning in turn the transport of sediment particles conveyed in the water, and, therefore, the resulting overbank sedimentation. The existence and pattern of sedimentation are conditioned by both the hydrodynamic variables (the flow-depth ratio and the width ratio) and the floodplain land cover simulated in terms of smooth walls, meadow-type roughness, sparse-wood-type roughness, and dense-wood-type roughness.

Key Points:
- Compound channel characteristics modulate the production of vertically axised large vortical turbulent structures in the mixing interface
- The morphological evolution of the floodplain is mainly controlled by the large vortices generated in the mixing interface
- The width ratio primary modulates the scale of the quasi-2-D vortical structures and ultimately, the overbank sedimentation

Correspondence to:
C. Juez,
carmelo.juez@upm.es

Citation:
Juez, C., Schärer, C., Jenny, H., Schleiss, A. J., & Franca, M. J. (2019). Floodplain land cover and flow hydrodynamic control of overbank sedimentation in compound channel flows. *Water Resources Research*, *55*. https://doi.org/10.1029/2019WR024989

Received 13 FEB 2019
Accepted 5 OCT 2019
Accepted article online 30 OCT 2019

1. Introduction

Floodplains in compound channels have a fundamental role in flood protection; they provide retention storage for flow regulation and they allow the deposition of deadwood and sediments. Furthermore, floodplains have an important natural function as the main connectors between the inland and the main channel of the river and by favoring the deposition of fine sediments rich in nutrients; therefore, floodplain areas are prone to colonization by riparian vegetation (Benjankar et al., 2011).

A fine balance between the feeding of new sediment and the extraction of old sediment (containing organic waste) is essential for the maintenance of the ecosystem functions of floodplains. An excess of overbank sedimentation may jeopardize the total conveyance capacity of the compound channel by changing the floodplain topography and the ecological processes that floodplains ensure (Benjankar et al., 2011). This excess of overbank sedimentation has become a major concern in recent years in glacier-fed streams (such as those in the Upper Rhône River in Switzerland), which transport fine sediments in suspension produced at the basal interface of a glacier. With increasing glacier melt due to climate change, the amount of fine sediments transported by glacier-fed rivers has increased dramatically. Furthermore, in river reaches governed by upstream dams, dam operations can cause an uncontrolled flushing of fine sediments accumulated in the reservoir, inducing an overabundance of these sediments (Tockner & Stanford, 2002).

There are several examples of field research on floodplains sedimentation from the past decades (Ahilan et al., 2016; Benjankar & Yager, 2012; Nicholas & Walling, 1997; Walling & Owens, 1998). However, the

results and conclusions of those works were site specific; thus, the generalization of their results regarding floodplain sedimentation is not possible given the variety of topographies, hydrodynamic conditions, suspended sediment concentration supplies, flood frequencies, flood durations, surface-water connectivity patterns (Czuba et al., 2019), and vegetation densities (Walling & Owens, 1998). Experimental work in laboratory compound channels allows us to reduce such complexity and to isolate and study individually, under controlled conditions, several processes, and variables that contribute to floodplain sedimentation. Thus, extensive research has been devoted to analyzing the flow of straight, compound channels in laboratories (see, e.g., the work in the Flood Channel Facility, Wallingford, UK, during the 1980s and 1990s; Knight & Shiono, 1990; Shiono & Knight, 1991). It is known that the difference in the water depth between the main channel and the floodplains is one of the main drivers of changes in the velocity gradient between the two subregions. This velocity gradient generates a mixing layer near the interface which, in turn, causes momentum exchange and ultimately reduces the discharge capacity compared with independent cross sections (i.e., there are three independent channels: one for the main channel and one for each lateral floodplain channel) (Sellin, 1964; Shiono & Knight, 1991). Most recently, researchers studied more complex geometries, such as compound channels with symmetrically narrowing channels (Bousmar et al., 2004; Proust et al., 2006) or skewed compound channels (Sellin, 1993). The obtained results highlighted the increase in the geometrical mass and momentum exchange between the main channel and the floodplains due to changes in the compound channel geometry (narrowing or skewed compound channels).

Furthermore, the flow-depth ratio between the water depth in the main channel and the water depth in the floodplain determine the formation of 2-D coherent, vertically axised macrovortices at the main channel/floodplain interface (flow structures responsible for mass and momentum exchanges are explained in the following laboratory studies; Bousmar et al., 2005; Proust et al., 2006) and thus to longitudinal and transversal mixing processes (Besio et al., 2012; Stocchino & Brocchini, 2010).

In nature, there are multiple types of floodplain vegetation coverage. Thus, the roughness of the floodplains depends on the vegetation land cover, which influences the velocity gradient between the main channel and the floodplain, the strength of the mixing layers, and the channel conveyance capacity. To date, several experimental campaigns have been carried out to study the influence of different vegetation roughness configurations on the flow: those on rough floodplains that mimic a meadow land cover vegetation (Dupuis et al., 2017; Fernandes et al., 2014; Shiono et al., 2009) and those on emergent tree-roughness elements (Dupuis et al., 2017; Koziol, 2013; White & Nepf, 2009). All these previous studies provide valuable insight into the possible prediction of the mass and momentum exchange processes in compound channels. These processes may be taken as a surrogate to determine the transport of fine sediments and ultimately, the floodplain sedimentation rates. However, this topic has never been fully and exclusively researched since experimental campaigns that include suspended fine sediment transport in compound channels are scarce and the data recorded during those campaigns are limited. The authors only found two other studies from the past 18 years: James (1985) and Bathurst et al. (2002). Both laboratory studies only measured and analyzed the final sediment deposition over the floodplains.

Here, we study experimentally the overbank sedimentation of fine sediments due to different hydrodynamic conditions and floodplain land covers. The compound channel under investigation is characterized by variables describing the hydrodynamics and morphodynamics: the flow-depth ratio between the water depth in the main channel and the water depth in the floodplain; the width ratio between the width of the main channel and the width of the floodplain; and the roughness type found in the floodplain, simulating different types of vegetation coverage. We aim to relate such characteristics with the resulting overbank sedimentation in terms of the two-dimensional free surface velocity and turbulence distribution, the mass exchange coefficients, the mass deposition, and the deposition patterns. Thus, the water depth, sediment concentration, sediment deposit mass, and area covered by the settled sediments were recorded throughout each experiment and were ultimately analyzed and discussed. We show that the combination of these compound channel characteristics modulates the production of vertically axised large turbulent vortical structures in the mixing interface which, in turn, determines the water mass exchange between the main channel and the floodplain conditioned on the overbank sedimentation.

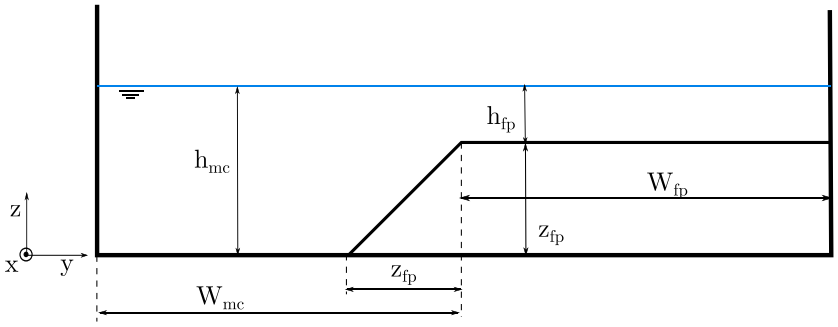

Figure 1. Sketch of the compound cross section. The lower and upper limits of the transition slope between the main channel and the floodplain are the channel/floodplain boundary.

2. Experimental Methods

2.1. Flume Description

Experiments were carried out in a recirculating flume. The flume is 13 m long, 1 m wide, and 1 m deep and consists of three parts: (i) an upstream mixing tank for supplying the discharge and suspended sediment, (ii) a rectangular channel with a 0.1% slope, and (iii) a downstream tank that collects the circulating flow and where a submerged pump is located. The discharge is measured by two parallel electromagnetic flowmeters. The water level is adjusted by a Venetian gate, which is located downstream at the end of the channel (see Juez, Buehlmann, et al., 2018, for more details). The length-to-width ratio of the flume is low, although within the range of values observed in other studies on compound channels in flumes (Bousmar et al., 2005; Shiono & Knight, 1991).

The flume cross section is asymmetrical, and it consists of a trapezoidal main channel (W_{mc}) and one lateral, flat floodplain (W_{fp}). The full depth of the bank in the main channel is constant ($z_{fp} = 3.5$ cm). Although the total flume width is fixed (1 m), the floodplain width is adjustable, and therefore, it allows the setup of different main channel widths. The x, y, and z axes are aligned with the streamwise, spanwise, and vertical direction of the flow, respectively, as illustrated in Figure 1. Both the main channel and floodplain bottoms are made of painted, smooth wood.

Experiments were performed under uniform flow conditions. To reduce the upstream nonuniform lateral mass exchange between the floodplain and the main channel, a stainless steel sheet was placed at the channel entrance (i.e., right after the upstream supplying tank) between the two subregions. In this way, the uniform flow conditions are achieved in a short downstream length. This technique was positively tested by two studies referenced in the manuscript: Azevedo et al. (2012) and Bousmar et al. (2005).

The upstream tank simultaneously supplies the main channel and floodplain regions, ensuring the same sediment concentration at the channel section inlet for the main channel and the floodplain. The flow depths and velocities in the main channel guarantee that the experiments were conducted under subcritical conditions. Furthermore, the Reynolds number (Table 1 notes the definition used for the *Re* calculation) is systematically above 4,000 in the main channel. However, the Reynolds number is below 4,000 in the floodplain region. This phenomenon is in agreement with other studies (Dupuis et al., 2016; Fernandes et al., 2014). It should be noted that in Fernandes et al. (2014), the Reynolds number is computed with the hydraulic diameter, whereas we use the hydraulic radius. Thus, the Reynolds number in our study is four times smaller. Furthermore, in Dupuis et al. (2016), the bulk variables were used, and therefore, no distinction is made between the main channel and floodplain region.

2.2. Experimental Design

The investigated compound channel configurations were asymmetric (i.e., the floodplain is on only one side of channel), and they were characterized by the following: (i) the flow-depth ratio between the water depth in the main channel (h_{mc}) and the water depth in the floodplain (h_{fp}): $r_h = h_{mc}/h_{fp}$; (ii) the ratio between the width of the floodplain (W_{fp}) and the width of the main channel (W_{mc}): $r_W = W_{fp}/W_{mc}$; and (iii) the different types of roughness on the floodplain. Table 1 displays the 24 compound channels tested.

When defining the flow-depth ratio, the classification provided by Nezu et al. (1999) was considered: shallow flows (SF, $r_h > 3$), intermediate flows (IF, $2 < r_h < 3$), and deep flows ($r_h < 2$). Since the situation of

Table 1
Summary of the Flow Conditions for Each Floodplain Configuration Tested

	$r_W = 1$		$r_W = 2$		$r_W = 3$		$r_W = 1$		$r_W = 2$		$r_W = 3$	
Flow condition	SF	IF	SF	IF	SF	IF	SF	IF	SF	IF	SF	IF
	Smooth roughness						Meadow-type roughness					
h_{fp} (cm)	1.75	3.00	1.75	3.00	1.75	3.00	1.75	3.00	1.75	3.00	1.75	3.00
h_{mc} (cm)	5.25	6.50	5.25	6.50	5.25	6.50	5.25	6.50	5.25	6.50	5.25	6.50
$r_h = h_{mc}/h_{fp}$	3.00	2.20	3.00	2.20	3.00	2.20	3.00	2.20	3.00	2.20	3.00	2.20
Q_{inlet} (L/s)	9.00	13.00	6.00	9.00	4.00	6.00	7.00	9.00	4.00	6.00	3.00	6.00
u_{fp} (m/s)	0.208	0.215	0.091	0.109	0.050	0.072	0.025	0.033	0.023	0.029	0.022	0.060
u_{mc} (m/s)	0.235	0.266	0.214	0.260	0.169	0.220	0.213	0.223	0.158	0.191	0.133	0.195
Fr_{fp} (−)	0.489	0.396	0.220	0.202	0.122	0.134	0.061	0.062	0.056	0.055	0.054	0.110
Fr_{mc} (−)	0.328	0.333	0.298	0.326	0.235	0.276	0.297	0.279	0.220	0.239	0.185	0.244
Re_{fp} (−)	3,315	5,765	1,515	3,023	1,242	2,932	418	910	392	823	555	2,419
Re_{mc} (−)	10,213	13,752	8,598	12,260	6,261	9,438	9,275	11,532	6,351	8,997	4,925	8,341
	Sparse-wood-type roughness						Dense-wood-type roughness					
h_{fp} (cm)	1.75	3.00	1.75	3.00	1.75	3.00	1.75	3.00	1.75	3.00	1.75	3.00
h_{mc} (cm)	5.25	6.50	5.25	6.50	5.25	6.50	5.25	6.50	5.25	6.50	5.25	6.50
$r_h = h_{mc}/h_{fp}$	3.00	2.20	3.00	2.20	3.00	2.20	3.00	2.20	3.00	2.20	3.00	2.20
Q_{inlet} (l/s)	7.00	9.00	4.00	6.00	3.00	5.00	7.00	9.00	3.00	6.00	3.00	5.00
u_{fp} (m/s)	0.013	0.024	0.014	0.027	0.017	0.031	0.013	0.020	0.014	0.028	0.016	0.031
u_{mc} (m/s)	0.204	0.216	0.142	0.207	0.126	0.205	0.201	0.213	0.130	0.210	0.126	0.205
Fr_{fp} (−)	0.032	0.038	0.031	0.049	0.041	0.057	0.031	0.037	0.033	0.051	0.022	0.031
Fr_{mc} (−)	0.270	0.248	0.202	0.236	0.167	0.246	0.279	0.256	0.185	0.051	0.175	0.057
Re_{fp} (−)	261	540	197	730	415	1,251	213	547	233	760	415	1,251
Re_{mc} (−)	8,862	11,191	5,724	9,743	4,663	8,775	8,726	10,489	5,219	9,412	4,663	8,348

Note. The experiments were grouped into four main categories depending on the floodplain land cover. Three width ratios, r_W, and two flow-depth ratios, r_h, were also considered. SF and IF stand for shallow and intermediate flows, respectively. The main flow variables for each test are displayed: h is the water depth; Q_{inlet} is the total flow rate supplied to the compound channel and recorded with the flowmeters; u is the longitudinal bulk flow velocity; $Fr = u/\sqrt{gh}$ is the Froude number; and $Re = R_h u/\nu$ is the Reynolds number, where R_h is the hydraulic radius and ν is the kinematic viscosity of the water. The subscripts mc and fp stand for the main channel and the floodplain, respectively. Accordingly, each flow variable was computed in the two regions present in the asymmetrical compound channel: the main channel and the floodplain.

deep flows is rare in nature, we consider only shallow and intermediate flows in this work. Conversely, the width ratio, r_W, is not related to a specific classification previously defined in the literature. In this study, this parameter ranges between 1 and 3. The width ratio determines the internal transverse shear instabilities due to lateral variations in the topography, which in turn modify the hydrodynamics of the channel (Nikora et al., 2007). Both the hydraulic and width ratios control the vorticity that participates in the mass and momentum exchange between the main channel and the floodplains (Jirka, 2001; Nikora et al., 2007; Stocchino & Brocchini, 2010).

Four types of floodplain roughness configurations were investigated, corresponding to different floodplain land covers (see Figure 2). We followed the previous work carried out by Dupuis et al. (2016, 2017), and we defined four types of bottom surfaces for the floodplains, while the main channel was kept smooth. The original smooth-channel bottom is made of painted wood to model a case where the roughness is the same in the floodplains and in the main channel (Manning's roughness coefficient $n = 0.01\ \mathrm{sm}^{-1/3}$); a plastic synthetic grass to model meadow-type vegetation in the floodplain (Manning's roughness coefficient $n = 0.075\ \mathrm{sm}^{-1/3}$); a plastic synthetic grass combined with a sparse distribution of wood cylinders to model a forest with sparse-wood-type vegetation in the floodplain (Manning roughness factor $n = 0.095\ \mathrm{sm}^{-1/3}$); and a plastic synthetic grass combined with a dense distribution of wood cylinders to model a forest with dense-wood-type vegetation in the floodplain (Manning roughness factor $n = 0.105\ \mathrm{sm}^{-1/3}$).

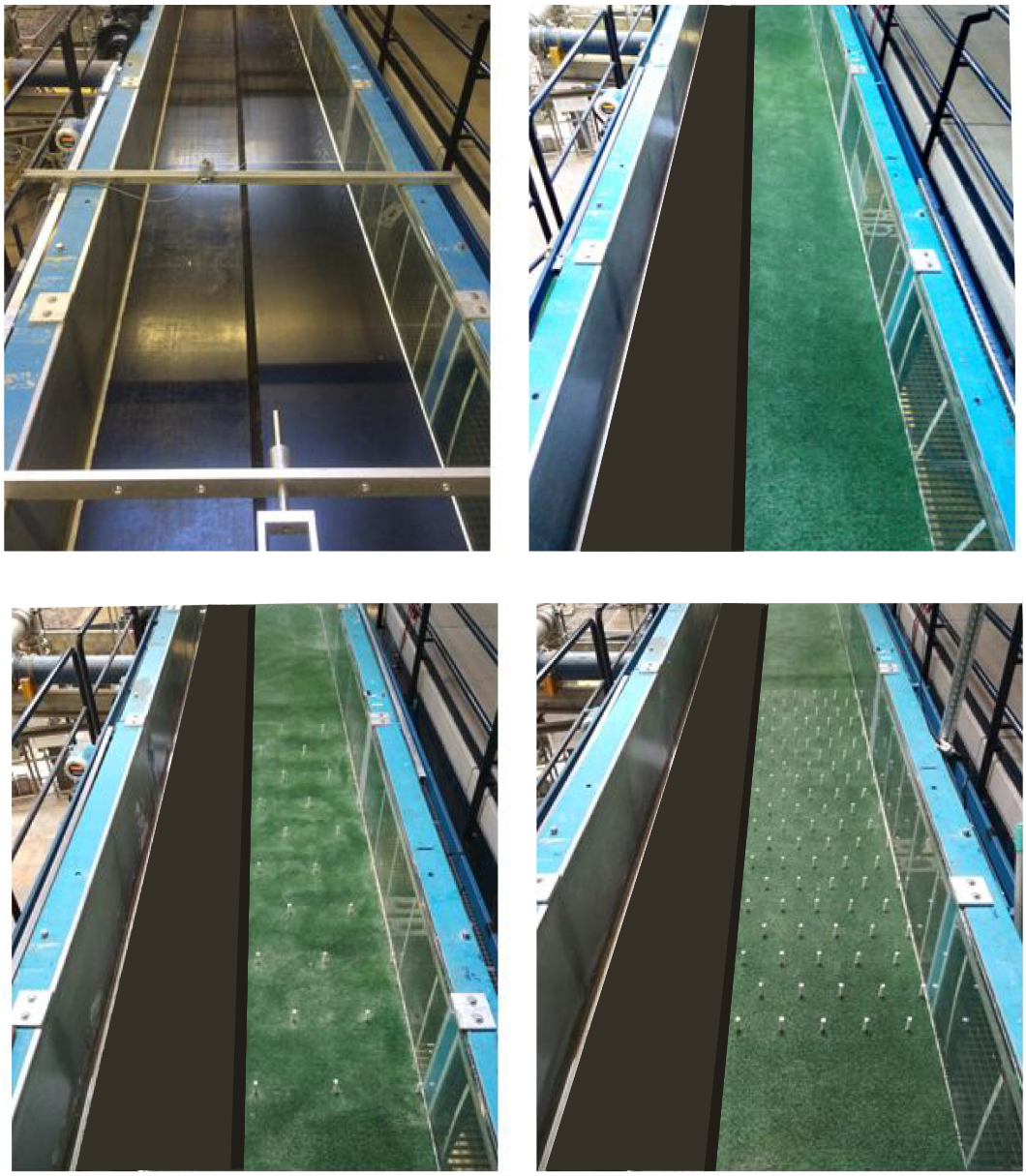

Figure 2. A bed roughness setup used in the experiments: smooth bed (top-left corner), meadow-type roughness (top-right corner), sparse wood-type roughness (bottom-left corner), and dense wood-type roughness (bottom-right corner).

The synthetic grass used was dense commercial grass, where the rigid blades of grass were 4 mm long. The wood-type vegetation was simulated using wood cylinders uniformly laid in staggered rows as in Dupuis et al. (2016, 2017). The diameter of the cylinder was 10 mm, and the spacing among cylinders was between 12 and 24 mm (depending on the dense or sparse wood vegetation test). Considering a 1:50 scale, these parameters correspond to a tree diameter of 0.5 m with a spacing between 6 and 12 m. Figure 3 illustrates the cylinder array. These values correspond well with the wood-type vegetation found in floodplains in the lower reaches of the Rhône River (Terrier, 2010).

To scale the suspended load transport, two possibilities exist: The first possibility consists of applying the geometrical similarity to the grain size of the prototype (i.e., $d_{50} = 0.2$ mm as found in suspension in Alpine rivers and documented by Federal Office of Environment, 2016). However, this results in very small sediment diameters when applying a spatial scale (e.g., a 1:10 scale implies a d_{50} in the model equal to 0.02 mm)

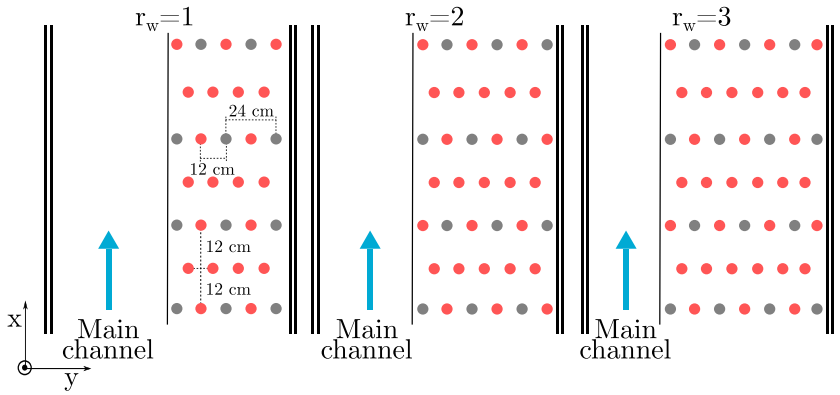

Figure 3. Top view of the wood-type configurations within the cylinder array. The gray cylinders correspond to the sparse distribution of wood-type vegetation. The combination of red and gray cylinders corresponds to the dense distribution of wood-type vegetation.

with the risk of cohesion among particles. The second possibility, and the one chosen in this work, consists of using a reduced density that reduces the settling velocity while maintaining the grain size. More details can be found in Yossef and de Vriend (2010) and Juez, Thalmann, et al. (2018). Therefore, the sediment used in the experiments was made from polyurethane; a similar artificial sediment has been used by authors of previous studies (Juez, Buehlmann, et al., 2018; Juez, Thalmann, et al., 2018; Juez, Marwan, & Franca, 2018). The grain size of the sediment was characterized by $d_{50} = 0.2$ mm, with a density equal to 1,160 kg/m^3. Cohesion problems were avoided since the sediment diameter fell in within the range of non-cohesive, fine sediment (62–500 μm; Van Rijn, 2007). Furthermore, the artificial nature of the sediments allows the avoidance of algae and biofilm growth.

The initial concentration of the fine suspended sediments was chosen to meet the maximum transport capacity of the flow for a channel without floodplains, that is, a flow the occupies the whole width of the channel. Two values of the initial sediment concentration were experimentally determined: 0.7 g/L for the shallow flow tests and 0.8 g/L for the intermediate flow tests.

2.3. Measurements

Water levels were measured all through the experiments by a Baumer ultrasonic probe. This device has a scanning range between 2 and 82 mm and a resolution below 0.3 mm. We used a sampling frequency of 10 Hz. Differences in the water levels among the measured sections were less than 2%; thus, the uniform flow condition was assumed. Furthermore, the flow rate was also monitored by an electromagnetic flowmeter located in each of the two existing supply pipes.

Surface velocities were measured with a 2-D surface particle image velocimetry (PIV) technique as in Juez, Buehlmann, et al. (2018) and Juez, Thalmann, et al. (2018). This PIV technique consisted of tracking the position of floating particles with a camera filming from above at a frequency of 60 Hz. The acquisition time was several times faster than the turbulence features generated at the shear layer (Kimura & Hosoda, 1997). This criterion ensured that the turbulence feature measurements were accurately recorded. Floating polypropylene particles with a diameter of 3 mm and a density of 0.946 g/L were used as tracers for the PIV. According to Weitbrecht et al. (2002) and based on the diameter of the tracers, our experimental setup could adequately detect flow structures with a minimum size of 5 times the diameter of the tracers (i.e., approximately 15 mm). Furthermore, a particle dispenser was used to seed the flow with a homogeneous density of particles floating on the water surface. Instantaneous and mean velocities were computed for a 2.0-m-long study reach, which was located 3.5 m downstream the channel inlet. Results from the surface PIV were postprocessed to infer the main flow characteristics. An ensemble average on the velocity fields and, then, spatial averages along the longitudinal direction were thus applied to obtain the cross-sectional distribution of the streamwise velocity, $\bar{u}$, and the Reynolds shear stresses per water density, $\overline{u'v'}$. Additionally, the mixing layer was also determined.

The temporal evolution of the suspended sediment concentration was recorded in the channel by two COSMOS-25 turbidimeters; one turbidimeter (Turbidimeter T1) was located upstream of the study reach,

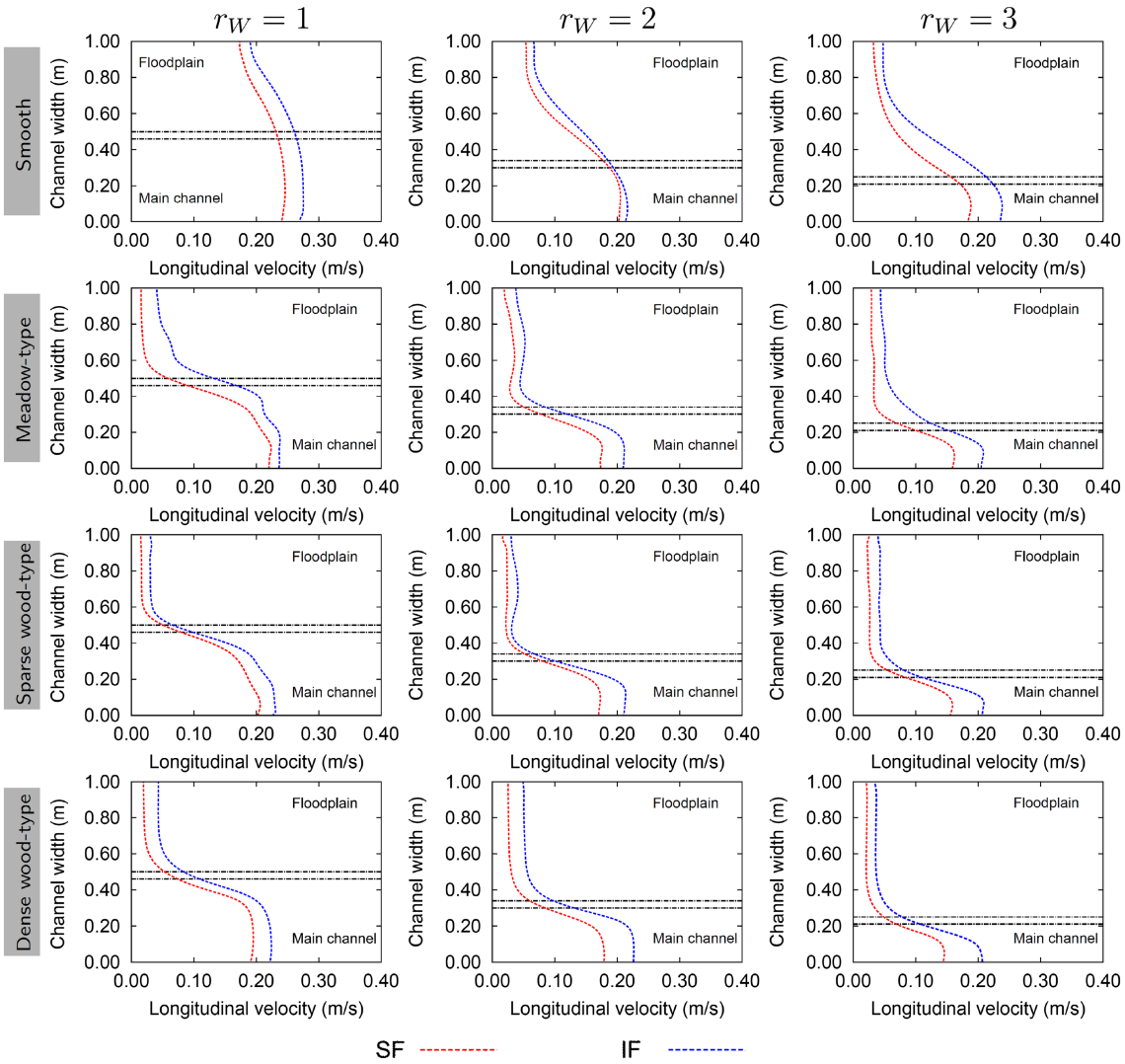

Figure 4. Cross-sectional distribution of the streamwise velocity for the different floodplain land covers and flow conditions. Dashed lines indicate the boundaries between the main channel and the floodplain, that is, the lower and upper limits of the transition slope between the main channel and the floodplain. SF and IF stand for shallow and intermediate flows, respectively.

and the other turbidimeter (Turbidimeter T2) was located downstream of the study reach. Both turbidimeters were located in the middle of the main channel. The signals were sampled at a frequency of 100 Hz and were subsequently averaged over 30 time steps. The information provided by the turbidimeters is pointwise, corresponding to a value in the vertical concentration profile. It was experimentally checked that the chosen vertical position of the turbidimeter ensured that the measured values corresponded roughly to the averaged concentration of the vertical profile for the initial sediment concentration (i.e., 0.7 g/L for the shallow flow conditions and 0.8 g/L for the intermediate flow conditions).

Plan view photos of the sedimentation patterns in the compound channel were taken at the end of the experiments after draining all the water of the channel. These photos were subsequently treated at the end of the experiments to extract the surface occupied by the sediments. Furthermore, at the end of the tests, the sediment mass that settled within the study reach was collected in a sampling grid of 0.05×0.05 m. The longitudinal and transversal sediment pattern distribution (i.e., the total sediment mass settled and surface occupied by the sediments, respectively) was thus assessed.

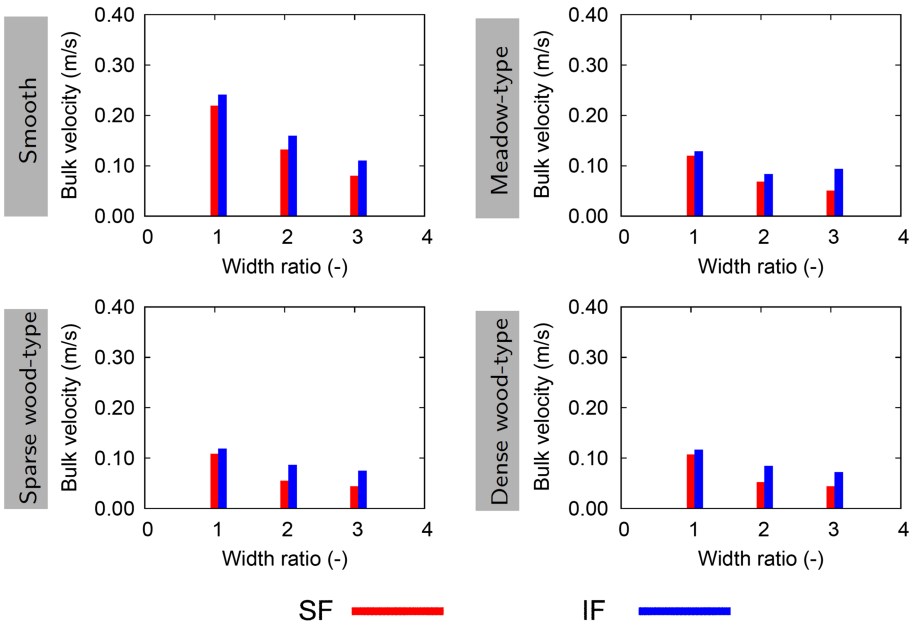

Figure 5. Mean bulk flow velocity of the compound cross section (main channel and floodplain) for the different floodplain land covers and flow conditions. SF and IF stand for shallow and intermediate flows, respectively.

3. Flow Hydrodynamics

3.1. Cross-Sectional Distribution of the Streamwise Velocity Measured at the Flow Surface

Figure 4 illustrates the cross-sectional distribution of the streamwise velocity for the different floodplain land covers and flow conditions. Both shallow flows and intermediate flows present a monotonic velocity profile, regardless of the roughness and the width ratio: The velocity values recorded in the main channel decrease systematically and with a strong velocity gradient between the main channel and the floodplain. The monotonic profile is associated with the presence of 2-D macrovortices that are produced by the shearing between the flow in the main channel and the flow in the floodplain. This finding is in contrast with the findings from Stocchino and Brocchini (2010) and Nezu et al. (1999), where a nonmonotonic profile was found for the intermediate flows, but in agreement with later work by Proust et al. (2017; see Figure 3e in this latter work). It should be noted that the experimental design in Proust et al. (2017) was carried out in an asymmetrical flume, as is the case in the present work, and it had a vertical rather than a gradual transition from the main channel to the floodplain. In contrast, Stocchino and Brocchini (2010) used a symmetrical flume and considered a much broader range of flow-depth ratios.

In Figure 5, the mean bulk flow velocity of the compound cross section (main channel and floodplain) for the different floodplain land covers and flow conditions is displayed. A reduction of the velocity values is observed with increasing (i) floodplain roughness and (ii) width ratio. The first finding is related to the fact that rough configurations are more efficient in terms of extracting energy from the flow, for example, a

Table 2
Summary of the Velocity Ratios λ Between the Mean Velocity in the Main Channel (u_{mc}) and the Mean Velocity in the Floodplain (u_{fp}), $\lambda = u_{mc}/u_{fp}$, Listed for Each Floodplain Land Cover and Flow Conditions

	$r_W = 1$		$r_W = 2$		$r_W = 3$	
Floodplain configuration	SF	IF	SF	IF	SF	IF
Smooth	1.2	1.2	2.4	2.4	3.3	3.0
Meadow-type roughness	8.4	6.6	6.7	6.4	5.9	3.2
Sparse-wood-type roughness	15.4	10.5	9.3	7.2	7.5	6.3
Dense-wood-type roughness	15.5	10.7	12.0	7.8	7.5	6.6

Note. SF and IF stand for shallow and intermediate flows, respectively.

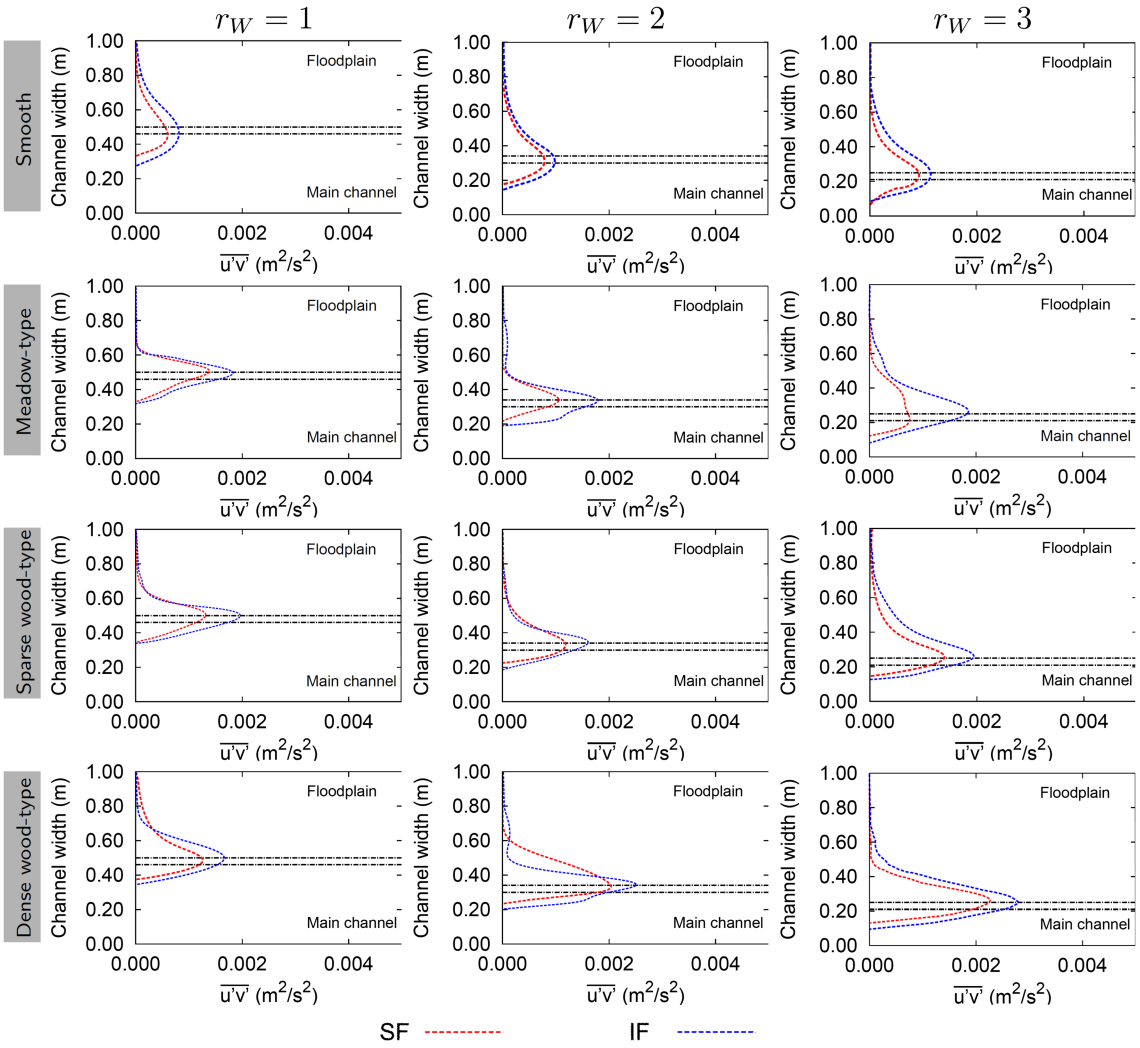

Figure 6. Cross-sectional distribution of the Reynolds shear stress profile for the different floodplain conditions. Dashed lines indicate the boundaries between the main channel and the floodplain. SF and IF stand for shallow and intermediate flows, respectively.

bottom frictional force for the meadow-type combined with drag force, in the case of wood-type floodplain land cover. The second finding is linked to the larger space that the floodplain occupies, which leads to a lower water level for the cross section (the discharge capacity in those configurations is lower). Furthermore, no differences are observed between shallow and intermediate flows, beyond the higher expected values of bulk velocity recorded for the intermediate flows.

Table 2 displays the velocity ratios between the mean velocity in the main channel (u_{mc}) and the mean velocity in the floodplain (u_{fp}), $\lambda = u_{mc}/u_{fp}$. The velocity ratio corresponding to the smooth floodplain is significantly smaller compared to that of the floodplains with a rough surface. The meadow-type and wood-type floodplains increase the roughness and, consequently, reduce the velocity of the flow in the floodplains and ultimately increase the velocity ratio. Sparse- and dense-wood-type floodplains display similar velocity ratios. The bottom frictional force is thus dominant over the drag force, and consequently, there are no significant differences between these two configurations.

Regarding the flow-depth ratio, the drop in the flow velocity over the floodplain due to the roughness is stronger for shallow flow conditions, where the velocity ratios between main channel and floodplain range from 1.2 (smooth configuration, $r_w = 1$) to 15.4 (dense-wood-type roughness, $r_w = 1$). For intermediate flow conditions, the velocity ratios are in the range between 1.2 (smooth configuration, $r_w = 1$) and 10.7 (sparse wood-type roughness, $r_w = 1$).

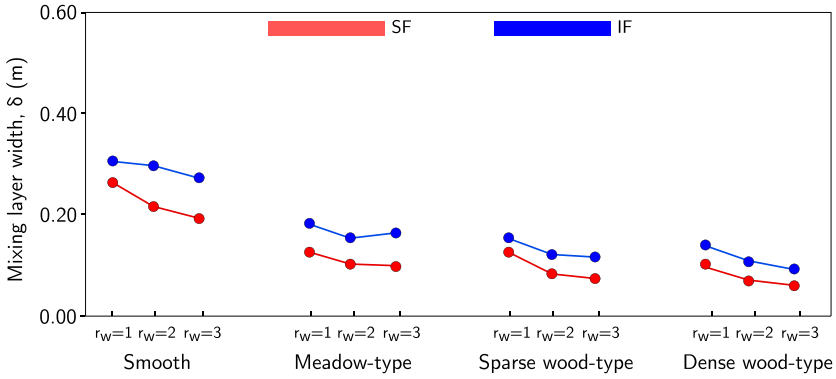

Figure 7. Mixing layer width, δ, for the different floodplain configurations. SF and IF stand for shallow and intermediate flows, respectively.

Additionally, we note that larger velocity ratios are observed for configurations with a width ratio of $r_w = 1$. According to Stocchino and Brocchini (2010), larger velocity ratios promote the intense production of macrovortices due to the strong shearing between the flow coming from the main channel and the flow coming from the floodplain.

3.2. Cross-Sectional Distribution of the Reynolds Shear Stress Measured at the Flow Surface

As outlined in Proust et al. (2017) the depth-averaged and time-averaged transverse exchange of streamwise momentum in a compound channel has three contributors: the depth-averaged Reynolds shear stress, the mean momentum transfer by the transverse flow, and the depth-averaged momentum transfer by secondary currents. The measurements obtained with the surface PIV only provide information concerning the motion of the free surface. Nevertheless, the shallowness of the configurations allows us to consider that the velocity field in the compound channel is mainly 2-D, and consequently, the results can be used as a proxy to understand the phenomena occurring in the whole water column. The depth-averaged Reynolds shear stress per water density in the water surface, $\overline{u'v'}$, can be inferred. Figure 6 displays the cross-sectional distribution of the Reynolds shear stress for all the hydrodynamic conditions and floodplain land covers.

In each case, the lateral profile depicts a bell shape with a maximum value in the boundary between the main channel and the floodplain. A strongest shearing is thus observed in the area of the compound channel. The Reynolds stresses are 0 close to the walls of the channel. The clear position of the peak in the transversal profile (inflection point) supports the existence of Kelvin-Helmholtz instabilities originating in the gradient of mean velocity between the two regions (see Figure 4) that ultimately form 2-D large coherent structures (Rayleigh's criterion, Huerre & Rossi, 1998).

The cases with rougher floodplains display higher shear stress peaks than the cases with smooth floodplains, regardless of the relative water depth (i.e., shallow or intermediate flow). Moreover, for intermediate flows, the magnitude of the shear stress is higher due to the higher velocities. We present shear stress measured at the water surface. Therefore, it is expected that close to the channel bottom, the shear stress presents lower values since it is a function of the relative vertical depth (Fernandes et al., 2014).

As the velocity ratio of the configurations decreases as the width ratio, r_w, increases (see Table 2), the maximum value of the shear stress increases. This phenomenon is clearly observed when comparing the configurations for which $r_w = 1$ and the configurations for which $r_w = 3$, regardless of the flow depth and the floodplain roughness. Additionally, the size of the bell shape of the shear stress profile tends to slightly shrink when the roughness of the floodplain increases. For example, for the configurations for which $r_w = 2$ in Figure 6, the shear stress profiles of the rough floodplain configurations (i.e., meadows, sparse wood, and dense wood) are narrower than the smooth floodplain configuration.

3.3. Mixing Layer

The velocity gradient between the flows in the main channel and in the floodplain induces the generation of a mixing layer at the channel-floodplain interface (also called the mixing interface; Shiono & Knight, 1991), which results in the shear production observed in Figure 6. It is in this region where the large turbulent coherent structures are developed. The mixing layer width can be defined based on the velocity gradient in

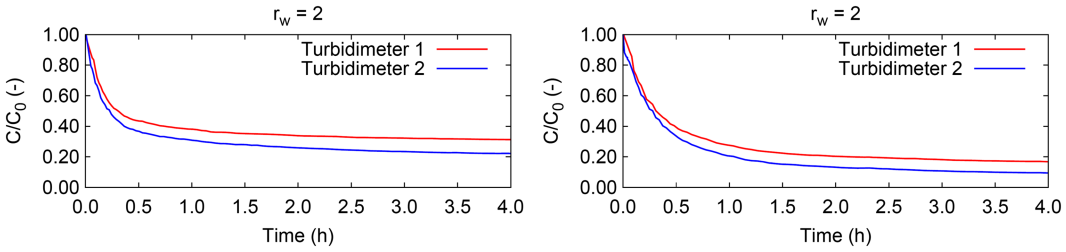

Figure 8. Temporal evolution of the normalized sediment concentration, c/c_0, for flow conditions with r_w=2 and smooth (left) and meadow-type roughness in the floodplain (right).

the compound channel. We follow the definition provided by Pope (2000) for free mixing layers:

$$\delta = \left| y_{0.9} - y_{0.1} \right| \tag{1}$$

where $y_{0.9}$ and $y_{0.1}$ are defined as the cross-sectional position at which the values of the streamwise velocity, $u_{0.9}$ and $u_{0.1}$, are obtained from the cross-sectional profiles (see Figure 4):

$$u_{0.9} = u_{fp} + 0.9\left(u_{\mathrm{mc}} - u_{\mathrm{fp}}\right) \qquad u_{0.1} = u_{\mathrm{fp}} + 0.1\left(u_{\mathrm{mc}} - u_{\mathrm{fp}}\right). \tag{2}$$

The upper limit of the mixing layer, $y_{0.9}$, is found in the vicinity of the interface between the main channel and the floodplain. The lower limit of the mixing layer, $y_{0.1}$, is always within the floodplain region.

Figure 7 illustrates the mixing layer width for the different configurations. For rough floodplains, the mixing layer is narrower than the smooth configurations. Even the configurations with sparse- and dense-wood-type roughness present a slight decrease in the mixing layer width compared with the meadow-type roughness. This finding is consistent with the findings from Fernandes et al. (2014). Moreover, lower width ratios (i.e., $r_w = 1$), which are linked with higher velocity ratios and an intense production of vortices, result in mixing layers that span in larger areas over the floodplain. This difference seems to attenuate with the increase in the water depth (intermediate flow), which is attributed to the decrease in the relative bottom roughness with respect to the water column. In addition, after comparing these results against those of the shear stress (see Figure 6), it is observed that smaller mixing layers associated with rough floodplains are linked to slightly narrower shear stress profiles.

4. Channel Morphodynamics

4.1. Morphological Equilibrium of the Experiments

Equilibrium of the experiments was assumed when the morphological changes in the channel were considered too small to be measured. To verify this equilibrium assumption, we focused on two variables: the sediment pattern distribution and the suspended sediment concentration.

The sediment pattern distribution was assessed by comparing the aerial photos of the study reach. It was therefore possible to determine the temporal evolution of the area occupied by settled sediments in the floodplains and in the main channel.

Furthermore, the suspended sediment concentration was recorded throughout the experiments at two streamwise positions within the main channel (upstream and downstream of the study reach), as explained earlier. The results belonging to two floodplain land covers (smooth and meadow-type roughness with $r_w = 2$) for both shallow flow and intermediate flow, normalized by the initial concentration (c/c_0), are plotted in Figure 8 as an example. Initially, the sediment concentration drops quickly, then it stabilizes and ultimately converges asymptotically to a quasi-equilibrium. This tendency was observed in all the experiments carried out.

The end of the experiments was considered the moment when minimal changes were observed in the sediment pattern distribution and in the suspended sediment concentration.

4.2. Turbulence Signature

Power spectral density (PSD) distributions of the suspended sediment concentration time series fluctuation were computed for the different experimental configurations (Figure 9). The data collected by the downstream turbidimeter (Turbidimeter T2, see Figure 8) in the middle of the main channel were used. Previous

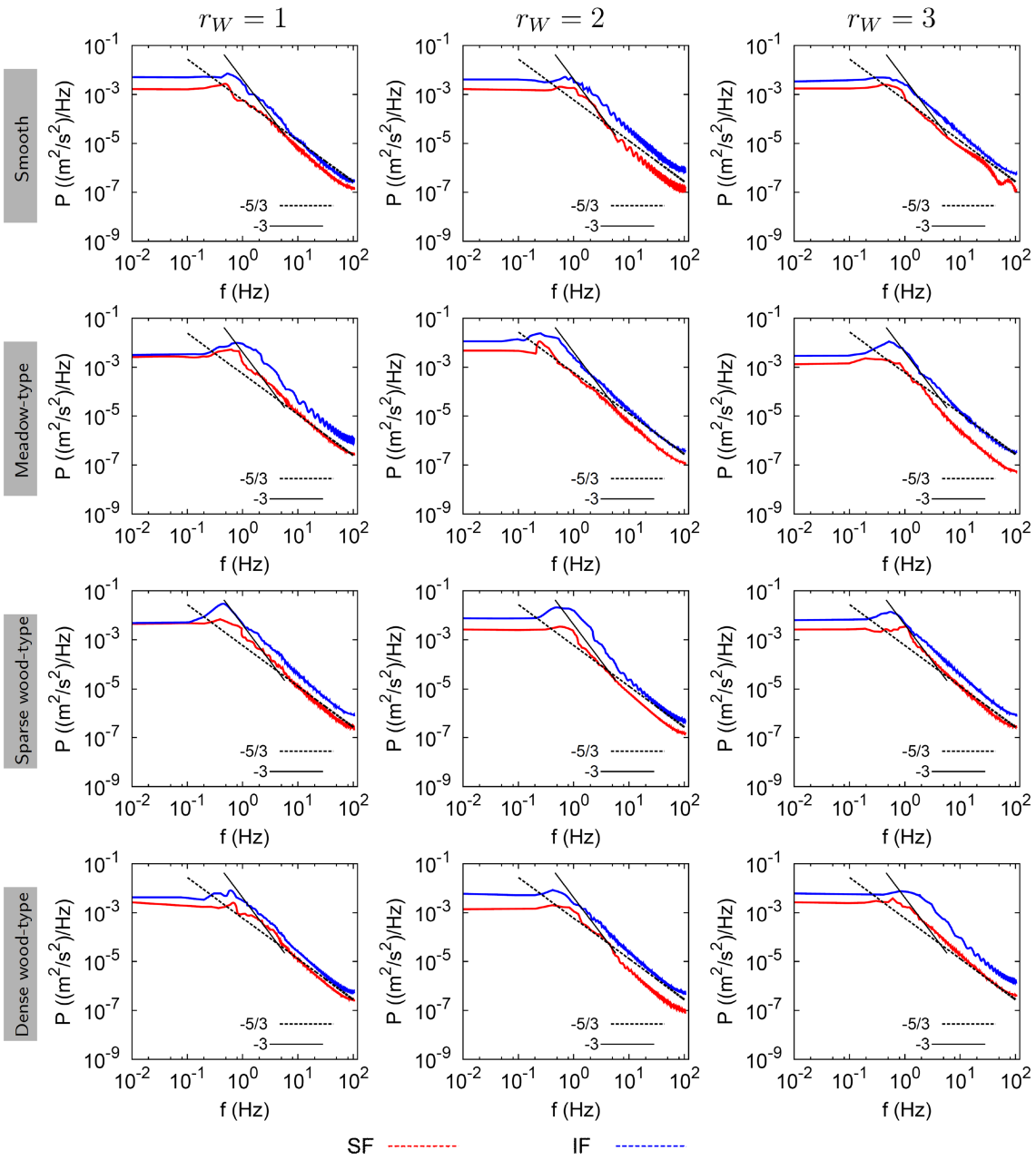

Figure 9. Distribution of the power spectral density of the suspended sediment concentration time series in the main channel for the different flow conditions and floodplain land covers. SF and IF stand for shallow and intermediate flows, respectively.

experimental studies were able to identify quasi-2-D and 3-D turbulent structures by means of the computation of the PSD: Both vortex structures were observed in unbounded shallow mixing layers (Jirka, 2001) and also in compound channel flows (Stocchino & Brocchini, 2010; Proust et al., 2017). Two-dimensional coherent structures are characterized by a scaling exponent of approximately −3 in the PSD distribution, in the middle range of frequencies, and by a scaling exponent of approximately −5/3 in the high-frequency range. The linear regression analysis we performed on our data set to determine such scaling exponents was statistically significant at the 95% confidence level, with correspondingly high coefficient of determination values, R^2 ($R^2 \geq 0.95$).

For all the configurations, the plots displayed in Figure 9 present a peak in the middle range of the energy spectra of the turbulence. This peak in the PSD distribution is adjacent to a region of the spectrum (toward the high frequencies) with a well-defined −3 scaling exponent. In the case of the shallow flow configurations

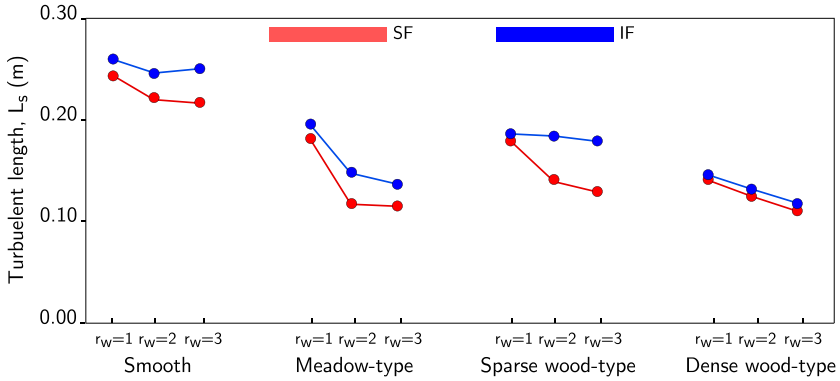

Figure 10. Turbulent length scales, L_s, for the different flow conditions and floodplain land covers. SF and IF stand for shallow and intermediate flows, respectively.

and smooth floodplains, the peak is generally less pronounced. For higher frequencies, the $-5/3$ scaling exponent corresponding to the inertial range of the PSD distribution is observed. It should be noted that within this range, both hydraulic conditions (shallow and intermediate) collapse reasonably well, which indicates that at the highest frequencies, the production of turbulent eddies is not affected by the flow-depth ratios used herein.

Additionally, a turbulence length scale, L_s, which is related to the size of the eddies, was also calculated: $L_s = u_{\mathrm{mc}}/f_s$, where u_{mc} is the mean velocity, which, in our case, is the bulk velocity in the main channel, and f_s is the frequency where the slope changes toward a $-5/3$ decay (i.e., the separation point between the saturation and scaling regions; Nikora et al., 2007). The results are displayed in Figure 10. The defined turbulence length scale ranges between 0.26 m (smooth floodplain configuration) and 0.11 m (dense-wood-type vegetation), that is, at scales larger than the flow depth. Rough floodplains present smaller turbulent length scales than the smooth configurations. Furthermore, and as reported by Nikora et al. (2007) for shallow mixing layers, the size (or scale) of the eddies increases with the Froude number: A configuration with $r_w = 1$ presents larger velocities and, therefore, a larger Froude number than a configuration with $r_w = 3$. This phenomenon ultimately leads to larger turbulent length scales for configurations for which $r_w = 1$.

The size of the turbulent length scale is related to the size of the mixing layer (see Figure 7). As is explained in Proust et al. (2017), the quasi-2-D structures facilitate the momentum transfer by turbulent mixing between the main channel and the floodplains. Therefore, larger quasi-2-D structures lead to a larger mixing layer, which is evidenced when looking at Figures 7 and 10: The smooth configurations display the larger mixing layer and the larger turbulent length, respectively. Moreover, the ratio of both scales, L_s/δ, in our experiments ranges between 0.7 and 1.5. Previous studies have reported larger values: $L_s/\delta \approx 3.5$ in Uijttewaal and Booji (2000) for shallow mixing layers, $L_s/\delta > 4$ in Dupuis et al. (2017) for compound channels with rough floodplains and $L_s/\delta > 4$ in Proust et al. (2017) for compound channels with nonuniform flows. The lower values of this ratio obtained in our work are justified by the fact that in previous studies, the PSD was applied to the velocity measurements recorded on the water surface of the mixing layer. Instead, we used the data recorded by the turbidimeters at a height lower than the water depth and located in the middle of the main channel. Therefore, the scale of the turbulent quasi-2-D structure is expected to be smaller due to the frictional effect of the bottom and also because it is further away from the mixing layer.

4.3. Exchange Coefficients

The mass exchange between the main channel and the floodplains for the different experimental conditions was determined by means of the 1-D mass exchange model presented by Valentine and Wood (1979). This classic model was originally proposed to determine the mass exchange of a pollution cloud, defined in terms of the concentration of a pollutant, between the main stream and a lateral cavity (see also Juez, Thalmann, et al., 2018; Weitbrecht et al., 2008). In our case, we can define the temporal evolution of the suspended sediment concentration in the main channel, C_{mc}, which is related to the mass exchange between the main channel and the floodplain, as

$$\frac{dC_{\mathrm{mc}}}{dt} = K_{\mathrm{mc\text{-}fp}}\left(C_{\mathrm{fp}} - C_{\mathrm{mc}}\right), \tag{3}$$

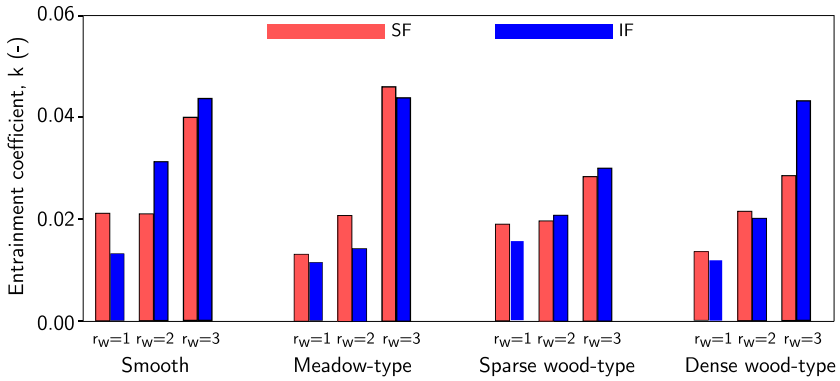

Figure 11. Dimensionless entrainment coefficients, k, for the different floodplain configurations. SF and IF stand for shallow and intermediate flows, respectively.

where C_{fp} is the suspended sediment concentration in the floodplain and $K_{mc\text{-}fp}$ (1/time) is the ratio between the exchanged volume per unit of time provided by the main channel, Q_{mc}, and the floodplain volume, V_{fp}:

$$K_{mc\text{-}fp} = \frac{Q_{mc}}{V_{fp}} = \frac{lh_{mc}E}{lW_{fp}h_{fp}} \tag{4}$$

where l is the length of the river reach along which the floodplain is connected to the main channel; h_{mc} the water depth in the main channel; E the exchange velocity; W_{fp} the width of the floodplain, and h_{fp} the water depth in the floodplain. Following Valentine and Wood (1979), the exchange velocity, E, has been normalized by the mean velocity in the main channel, U_{mc}, leading to a dimensionless entrainment coefficient: $k = E/U_{mc}$. This entrainment coefficient is replaced in (4), and subsequently, equation (4) is substituted in (3). Thus, equation (3) reads as follows:

$$\frac{dC_{mc}}{dt} = \frac{kU_{mc}r_h}{W_{fp}}\left(C_c - C_m\right) \quad \text{where} \quad r_h = \frac{h_{mc}}{h_{fp}}. \tag{5}$$

Ultimately, the integration of equation (5) leads to the definition of the temporal evolution of the suspended sediment concentration:

$$C_{mc} = Ae^{-\left(\frac{kU_{mc}r_h}{W_{fp}}\right)t} + B \tag{6}$$

where A and B are two constants. The dimensionless entrainment coefficient, k, accounts for the amount of suspended sediment exchanged between the main channel and the floodplain.

To determine experimentally the dimensionless entrainment coefficient, k, the time series sediment concentration decay recorded by the two turbidimeters was used. The averaged value of the temporal decay provided by both turbidimeters was computed. The data were normalized by the initial concentration of the experiments (C_0). The resulting sediment concentration data were fitted by an exponential decay of the first order: $C = Ae^{(-Dt)} + B$. The exponential regressions for this analysis were statistically significant at the 95% confidence level, with high R^2 values ($R^2 \geq 0.90$). The coefficient D from the exponential fit corresponds to the term $\left(kU_{mc}r_h\right)/W_{fp}$ in equation (6). Therefore, the entrainment coefficient values, k, were calculated and are displayed in Figure 11 for all the experimental configurations.

The values among the different roughness are relatively similar and are on the same order of magnitude. We can thus infer that overbank sedimentation is not only driven by the increase in roughness.

The differences between the values of the entrainment coefficient, k, for the different floodplain land covers are neither significant nor conclusive. Hence, in the range of experimental conditions tested, the floodplain land cover (i.e., the roughness) seems to be irrelevant for the overbank sedimentation levels.

Instead, the velocity ratio (see Table 2) seems to play an important role in the mass exchange between the main channel and the floodplain. The levels of turbulence verified in the mixing layer between the main channel and the floodplain depend directly on the velocity ratio. Higher velocity ratios lead to higher turbulence intensities (i.e., larger vortical structures in the mixing layer, see Figure 10) and to stronger conditions

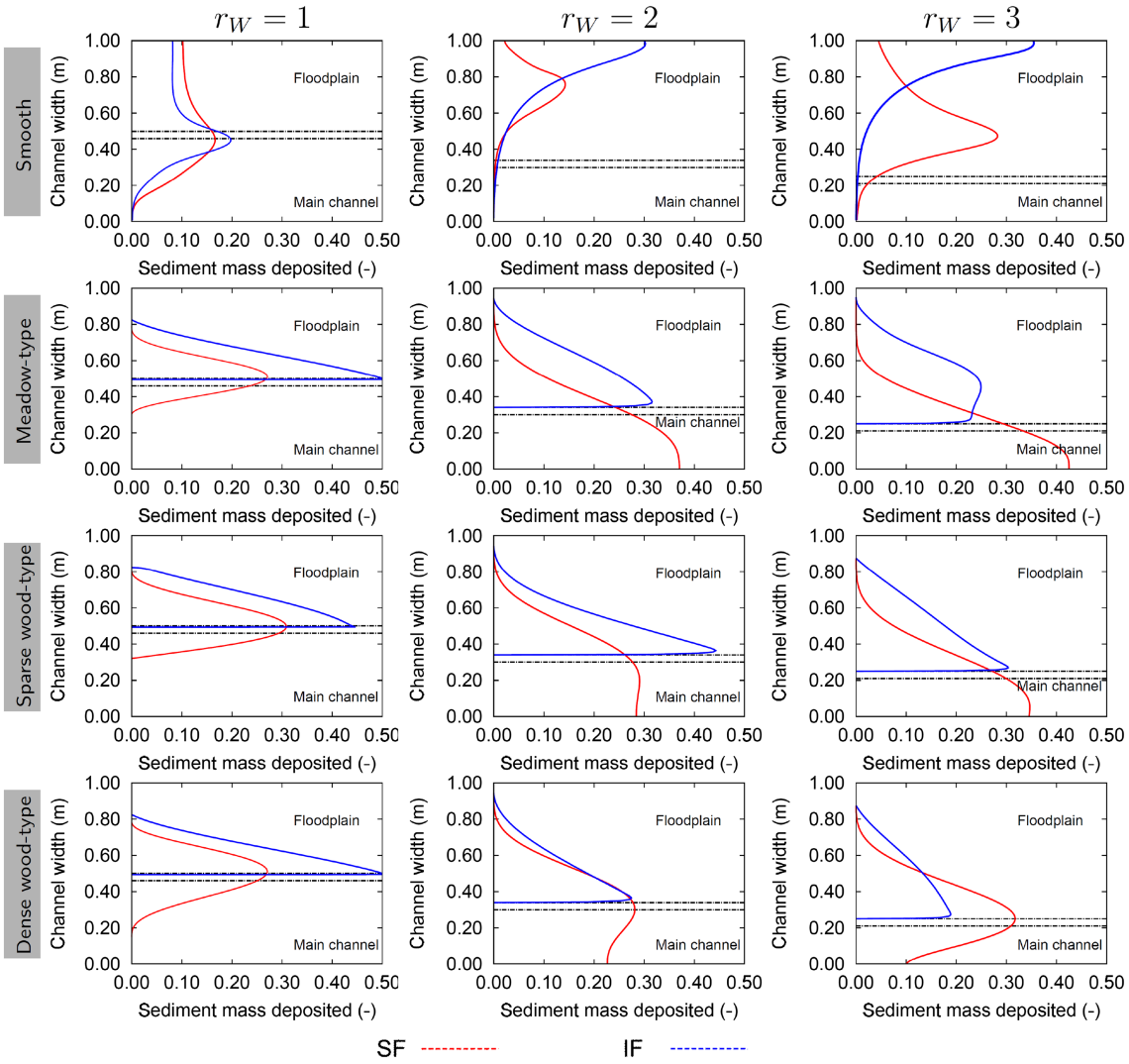

Figure 12. Cross-sectional sediment mass distribution at the end of the experiment for the different floodplain configurations. Dashed lines indicate the boundaries between the main channel and the floodplain. SF and IF stand for shallow and intermediate flows, respectively.

for the suspension of sediments hindering their deposition and allowing their downstream transport by the longitudinal mean flow.

In light of the varying flow depth, it seems that the different values of the entrainment coefficient, k, are related only to the ratio between the velocities in the main channel and the floodplain in the same manner as observed earlier when analyzing the influence of the floodplain land cover.

However, the relevance of the width ratio, r_w, in determining the values of the entrainment coefficient, k, is clear. A narrower main channel and wider floodplain (i.e., $r_w = 3$) are related to a larger entrainment coefficient regardless the flow-depth ratio and the floodplain land cover. For the experimental conditions tested, the width ratio is the parameter that most relates to the velocity ratio; hence, it is natural that r_w is the parameter that is the best at explaining the observed overbank sedimentation.

4.4. Sediment Mass Distribution

At the end of each experiment, the sediment mass deposited in the channel within the study reach (floodplain and main channel) was collected in a sampling grid of 0.05 × 0.05 m, dried and weighed.

For the smooth and meadow-type roughness conditions, regardless of the width ratio and hydraulic flow conditions, no longitudinal variation was observed within the study reach. This finding is not surprising since the experiments were carried out under uniform flow conditions. However, for the sparse- and dense-

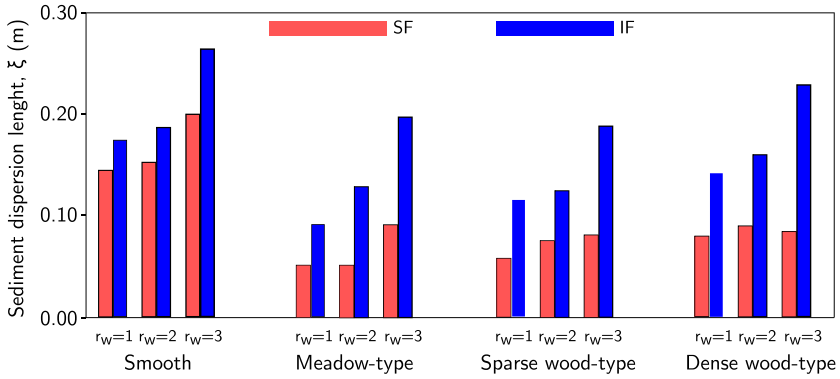

Figure 13. Sediment dispersion length for the different floodplain configurations. SF and IF stand for shallow and intermediate flows, respectively.

wood-type vegetation, a slight decrease (10–15% less) of the settled mass along the floodplains within flow direction was obtained. This decrease is more pronounced for the configurations with the dense-wood-type roughness and wider floodplains. This impact of trees on the longitudinal sediment mass distribution is linked to the drag force exerted by the trees in the flow. Further downstream of the study reach, the accumulation of trees (and their drag effect) favors the settling of sediments.

Additionally, the sediment samples collected at the end of the experiment were normalized by the total sediment mass collected within the study reach. The cross-sectional sediment mass distributions at the end of the experiment for the different floodplain configurations are displayed in Figure 12.

The cross-sectional sediment mass distribution displays a different behavior between smooth and rough floodplain configurations. For the smooth configurations, the sediment mass spans deeper into the floodplain region. For the intermediate flow and smooth cases, the peak of the sedimentation is found in the vicinity of the floodplain channel wall. In the rough floodplain configurations (i.e., meadow, sparse-wood-type and dense-wood-type roughness), the sediment patterns among them are quite similar. In the shallow flow experiments, settled sediments are observed in the main channel and in the floodplain. In contrast, in the intermediate flow experiments, only overbank sedimentation is observed and the peak of such sedimentation and corresponds well with the location of the mixing interface. Additionally, the sediments settle deeper into the floodplain than under shallow flow conditions.

Regarding the width ratio, r_w, a slight increase in the spanning area into the floodplain in $r_w = 3$ is observed compared to configurations for which $r_w = 1$ and $r_w = 2$.

The observed deposition patterns for rough floodplains correspond well to the ones found in real floodplains (Asselman & Middelkoop, 1995) and in two laboratory experiments (Bathurst et al., 2002; James, 1985). These previous studies similarly found that the sediment dispersion spanning into the floodplain is weak, and thus, the overbank sedimentation is limited to the area close to the mixing interface. Furthermore, these experimental results correspond well to natural levee sedimentation observations: The distance at which sediments are transported across the floodplain surface is not far from the mixing layer, mainly due to the floodplain vegetation (meadow-type and wood-type test cases in our experimental campaign), which results in a higher flow resistance (Hudsoni, 2005).

Additionally, the distance between the center of mass of the sedimentation patterns and the mixing interface, ξ, was determined. This variable can serve as a proxy to assess the sediment dispersion into the floodplain region (similar to a sediment dispersion length). The results are displayed in Figure 13.

The smooth configurations depict larger sediment dispersion lengths with respect to the rough configurations. This finding is attributed to the fact that the frictional force in rough floodplains reduces the floodplain velocity, and therefore, overbank sedimentation occurs closer to the main channel. Moreover, differences among the rough configurations are not noticeable.

Conversely, the sediment dispersion length is significantly impacted by the width ratio and the flow conditions. For , with deeper overbank flows, the dispersion of the sediments in the floodplain region is larger than

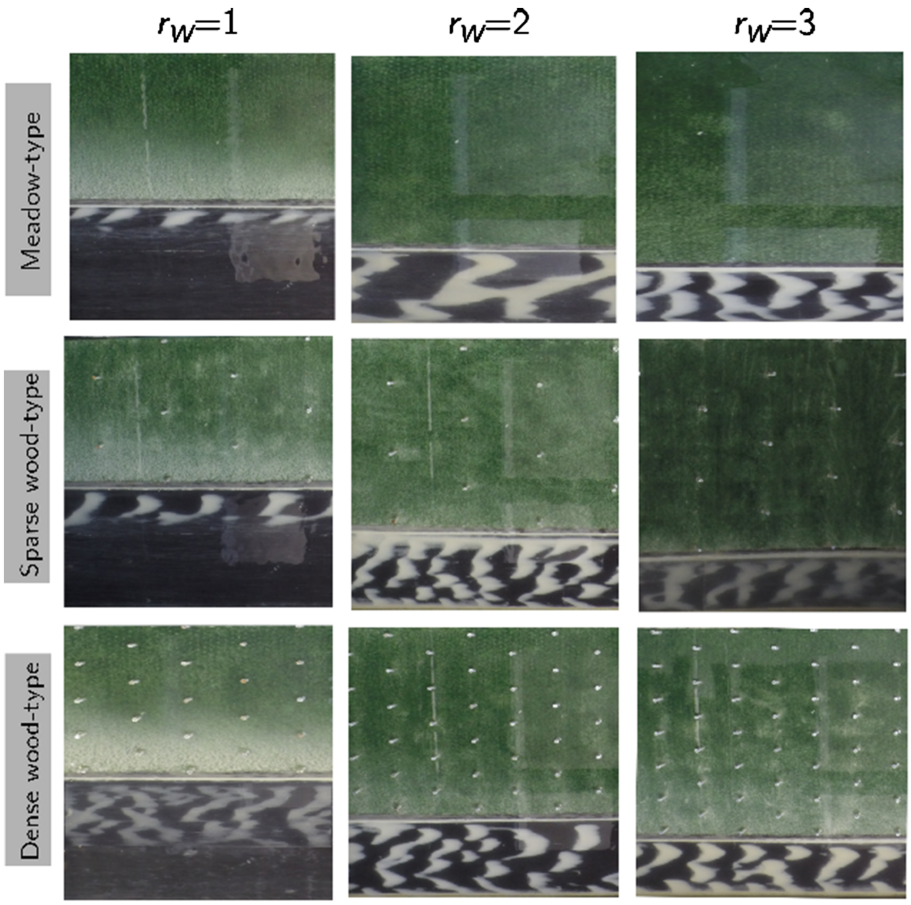

Figure 14. Top view of the bedforms over the channel for the rough floodplain configurations and under shallow flow conditions. Fine sediments are white, and the bottom of the channel was painted black.

that in the shallow flow conditions. Furthermore, the sediment dispersion length is larger for configurations for which $r_w = 3$ than for configurations for which $r_w = 1$ and $r_w = 2$.

4.5. Bed Forms

The formation of bedforms in the main channel was observed in the shallow flow conditions and rough configurations. Figure 14 displays the top view of the bedforms over the channel. For wider floodplains, configurations with the width ratio of $r_w = 2$ and 3, the bedforms covered the whole width of the main channel. In contrast, for $r_w = 1$, the bedforms partially occupy the main channel and are located in the vicinity of the mixing interface region.

The wavelengths of the bedforms were computed. They ranged between 0.08 and 0.25 m, which corresponds to a 1.4–4.3-fold increase in the water height in the main channel under shallow flow conditions. According to the criteria from Yalin (1985), the observed wavelengths of the bedforms equal the expected wavelengths for ripples. Upscaling these ripples to a field case, which should be much larger in dimensions that the flume used herein, implies that these bedforms fall in the category of large dunes.

To assess the possible influence of the bedforms as a macroroughness element of the flow, hence affecting its main structure, PIV measurements were also carried out at the end of the experiments. No effect on the flow patterns due to the presence of ripples was observed.

5. Discussion

We conducted compound channel experiments to explore the role of (i) the flow-depth ratio between the water depth in the main channel and the water depth in the floodplain; (ii) the width ratio between the width

of the main channel and the width of the floodplain; and (iii) the floodplain roughness, in the exchange dynamics of water and fine sediments between the main channel and the floodplain.

The exchange processes of water and fine sediments in suspension between the main channel and the floodplain were primarily influenced by the width ratio (r_w) and the hydraulic flow conditions (shallow and intermediate flows analyzed herein) and were secondarily influenced by the roughness.

The increase in the width ratio, r_w, is linked with the decrease in the velocity ratio, λ (see Table 2). As a result, the mixing layer width, δ, is also reduced (see Figure 7), and ultimately, the turbulent length scales are also smaller (see Figure 10). This finding is in agreement with van Prooijen and Uijttewaal (2002) and Stocchino and Brocchini (2010): the quasi-2-D structures found in the region of the mixing interface scale with the shear layer width. These findings are valid for the two flow-depth ratios tested herein.

The vortical production in the mixing layer is closely linked with the overbank sedimentation patterns; larger width ratios (e.g., $r_w = 3$) result in larger sedimentation rates (i.e., larger entrainment coefficients, k, see Figure 11) and also in larger sediment dispersion lengths over the floodplain (see Figure 13). This phenomenon is related to the fact that for larger width ratios, the mixing layer widths, and turbulent lengths are smaller. Consequently, the quasi-2-D vortices generated in the mixing layer are smaller (i.e., they are created and dissipate in a smaller length scale), and ultimately, the amount of sediments in suspension that settle in the floodplain is larger. In contrast, when the turbulence created in the mixing layer is higher (i.e., the experiments in which $r_w = 1$), the fine sediment particles travel further downstream within the large quasi-2-D mixing layer vortices and stay in suspension due to the turbulent energy provided by the larger vortices. The sediment exchange from the main channel to the floodplain is thus limited (sediments do not settle over the floodplain), and most of the particles are advected downstream by such large vortical structures, which are mainly contained within the main channel region.

Conversely, the dispersion of sediments settled over the floodplain is limited. This fact was already depicted by Bathurst et al. (2002) and James (1985) based in field studies. The amount of settled sediment decreases as we move into the floodplain and further away from the mixing interface. The sediment dispersion length, ξ, is larger for higher width ratios and under intermediate flow conditions. This phenomenon is attributed to the smaller size of the vortical structures in the case of configurations with larger width ratios. The sediments are not eventually advected downstream and the sediments span deeper over the floodplain.

The tests with different roughness configurations show that the change from a smooth floodplain to a rough meadow-type floodplain have an important relevance in the flow patterns: the flow velocity in both the main channel and the floodplain is decreased. However, the change from a meadow-type floodplain to a sparse- or dense-wood-type roughness displays a marginal impact. The frictional bottom roughness is thus dominant over the drag force attributed to the vertical stems.

6. Conclusions

In the present paper, an asymmetric compound channel conveying fine sediments was tested under configurations with different flow-depth ratio between the water depth in the main channel and the water depth in the floodplain; width ratios between the width of the main channel and the width of the floodplain; and roughness types found in the floodplain.

The morphological evolution of floodplains is mainly controlled by large vortices generated in the mixing interface, which promote or prevent the exchange of sediments between the main channel and the floodplain. The width ratio primary modulates the scale of the quasi-2-D vortical structures and ultimately the overbank sedimentation: Larger width ratios are linked to smaller vortices, and consequently, fewer fine sediments are transported downstream. Smaller vortices do not provide enough turbulence to keep the fine sediments in suspension, so they eventually settle over the floodplain.

The flow-depth ratios tested herein also shape the dispersion of sediments over the floodplain. Higher water depths over the floodplain (intermediate flow) allow the sediments to span deeper over the floodplain. The differences found among the rough floodplain configurations with and without vertical stems were not significant. We can thus conclude that the frictional bottom roughness (meadow roughness) is dominant over the drag force attributed to the vertical stems (sparse- and dense-wood-type roughness).

The results presented here are only valid for flows in straight, compound channels under uniform conditions with a limited variability in the flow-depth ratios. Further research should take into consideration the nonuniformity of the flow, broader flow-depth ratios and the possibility of a meandering channel geometry.

Acknowledgments
This work was funded by the FOEN (Federal Office for the Environment, Switzerland) under the framework of the *Lebensraum Gewaesser Sedimentdynamik Und Vernetzung* (Riparian Habitat and Sediment Dynamics Interaction) research project and the H2020-MSCA-IF-2018 program (Marie Sklodowska-Curie Actions) of the European Union under REA Grant Agreement 834329-SEDILAND. The data used are available upon request and are also included in the following repository: (https://enacshare.epfl.ch/f9ojY6KMvwDCmZS4EAnrQFa85suHGdf).

References

Ahilan, S., Guan, M., Sleigh, A., Wright, N., & Chang, H. (2016). The influence of floodplain restoration on flow and sediment dynamics in an urban river. *Journal of Flood Risk Management*, *92*, 1–16. https://doi.org/10.1111/jfr3.12251

Asselman, N. E., & Middelkoop, H. (1995). Floodplain sedimentation: Quantities, patterns and processes. *Earth Surface Processes and Landforms*, *20*(6), 481–499.

Azevedo, R., Leal, J., & Solrzano, R. (2012). Influence of vegetation on compound-channel turbulent field. In Taylor Francis Group (Ed.), *River flow 2012* (pp. 209–216). London, UK.

Bathurst, J., Benson, I., Valentine, E., & Nalluri, C. (2002). Overbank sediment deposition patterns for straight and meandering flume channels. *Earth Surface Processes and Landforms*, *27*(6), 659–665.

Benjankar, R., Egger, G., Jorde, K., Goodwin, P., & Glenn, N. (2011). Dynamic floodplain vegetation model development for the Kootenai River, USA. *Journal of Environmental Management*, *92*, 3058–3070. https://doi.org/10.1016/j.jenvman.2011.07.017

Benjankar, R., & Yager, E. M. (2012). The impact of different sediment concentrations and sediment transport formulas on the simulated floodplain processes. *Journal of Hydrology*, *450-451*, 230–243. https://doi.org/10.1016/j.jhydrol.2012.05.009

Besio, G., Stocchino, A., Angiolani, S., & Brocchini, M. (2012). Transversal and longitudinal mixing in compound channels. *Water Resources Research*, *48*, W12517. https://doi.org/10.1029/2012WR012316

Bousmar, D., Wilkin, N., Jacquemart, J. H., & Zech, Y. (2004). Overbank flow in symmetrically narrowing floodplains. *Journal of Hydraulic Engineering*, *130*(4), 305–312. https://doi.org/10.1061/(ASCE)0733-9429(2004)130:4(305)

Bousmar, D., Riviere, N., Proust, S., Paquier, A., Morel, R., & Zech, Y. (2005). Upstream discharge distribution in compound-channel flumes. *Journal of Hydraulic Engineering*, *131*(5), 408–412. https://doi.org/10.1061/(ASCE)0733-9429(2005)131:5(408)

Czuba, J. A., David, S. R., Edmonds, D. A., & Ward, A. S. (2019). Dynamics of surface water connectivity in a lowgradient meandering river floodplain. *Water Resources Research*, *55*, 1849–1870. https://doi.org/10.1029/2018WR023527

Dupuis, S., Proust, S., Berni, S., & Paquier, A. (2016). Combined effects of bed friction and emergent cylinder drag in open channel flow. *Environmental Fluid Mechanics*, *16*, 1173–1193. https://doi.org/10.1007/s10652-016-9471-2

Dupuis, S., Proust, S., Berni, S., & Paquier, A. (2017). Compound channel flow with a longitudinal transition in hydraulic roughness over the floodplains. *Environmental Fluid Mechanics*, *17*, 903–928. https://doi.org/10.1007/s10652-017-9525-0

Federal Office of Environment (2016). Hydrological data service for watercourses and lakes.

Fernandes, J. N., Leal, J. B., & Cardoso, A. H. (2014). Improvement of the lateral distribution method based on the mixing layer theory. *Advances in Water Resources*, *69*, 159–167. https://doi.org/10.1016/j.advwatres.2014.04.003

Hudsoni, P. (2005): Encyclopedia of Water Science:Natural levees. https://doi.org/10.1081/E-EWS-120038052

Huerre, P., & Rossi, M. (1998). *Hydrodynamics and nonlinear instabilities*. Cambridge University Press.

James, C. (1985). Sediment transfer to overbank sections. *Journal of Hydraulic Research*, *23*(5), 435–452.

Jirka, G. H. (2001). Large-scale flow structures and mixing processes in shallow flows. *Journal of Hydraulic Research*, *39*(6), 567–573.

Juez, C., Buehlmann, I., Maechler, G., Schleiss, A. J., & Franca, M. J. (2018). Influence of bank macro-roughness on the transport of suspended sediments. *Earth Surface Processes and Landforms*, *43*, 271–284. https://doi.org/10.1002/esp.4243

Juez, C., Marwan, M., & Franca, M. J. (2018). The origin of fine sediment determines the observations of suspended sediment fluxes under unsteady flow conditions. *Water Resources Research*, *115*, 5654–5669. https://doi.org/10.1029/2018WR022982

Juez, C., Thalmann, M., Schleiss, A. J., & Franca, M. J. (2018). Morphological resilience to flow fluctuations of fine sediment deposits in bank lateral cavities. *Advances in Water Resources*, *115*, 44–59. https://doi.org/10.1016/j.advwatres.2018.03.004

Kimura, I., & Hosoda, T. (1997). Fundamental properties of flows in open channels with dead zone. *Journal of Hydraulic Engineering*, *123*(2), 98–107.

Knight, D., & Shiono, K. (1990). Turbulence measurements in a shear layer region of a compound channel. *Journal of Hydraulic Research*, *28*(2), 175–196.

Koziol, A. (2013). Three-dimensional turbulence intensity in a compound channel. *Journal of Hydraulic Engineering*, *139*, 852–864. https://doi.org/10.1061/(ASCE)HY.1943-7900.0000739

Nezu, I., Onitsuka, K., & Iketani, K. (1999). *Coherent horizontal vortices in compound open channel flows, in Hydraulic Modeling* (pp. 17–32): Water Resources Publications.

Nicholas, A. P., & Walling, D. (1997). Investigating spatial patterns of medium-term overbank sedimentation on floodplains: A combined numerical modelling and radiocaesium-based approach. *Geomorphology*, *19*, 133–150. https://doi.org/10.1016/S0169-555X(96)00043-8

Nikora, V., Nokes, R., Veale, W., Davidson, M., & Jirka, G. H. (2007). Large-scale turbulent structure of uniform shallow free-surface flows. *Environmental Fluid Mechanics*, *7*, 159–172. https://doi.org/0.1007/s10652-007-9021-z

Pope, S. (2000). *Turbulent flows* (pp. 139–144): Cambridge University Press.

Proust, S., Fernandes, J. N., Leal, J. B., Riviere, N., & Peltier, Y. (2017). Mixing layer and coherent structures in compound channel flows: Effects of transverse flow, velocity ratio and vertical confinement. *Water Resources Research*, *53*, 3387–3406. https://doi.org/10.1002/2016WR019873

Proust, S., Riviere, N., Bousmar, D., Paquier, A., Zech, Y., & Morel, R. (2006). Flow in compound channel with abrupt floodplain contraction. *Journal of Hydraulic Engineering*, *132*(9), 958–970. https://doi.org/10.1061/(ASCE)0733-9429\ignorespaces(2006)132:9(958)

Sellin, R. H. J. (1964). A laboratory investigation into the interaction between the flow in the channel of a river and that over its floodplain. *Houille Blanche*, *20*(7), 793–801.

Sellin, R. H. J. (1993). *Serc flood channel facility. Experimental data, Phase A. Straight two-stage channels. Skewed floodplain boundaries*. Bristol, UK: University of Bristol.

Shiono, K., Chan, T. L., Spooner, J., Rameshwaran, P., & Chandler, J. H. (2009). The effect of floodplain roughness on flow structures, bedforms and sediment transport rates in meandering channels with overbank flows: Part I. *Journal of Hydraulic Research*, *47*, 5–19. https://doi.org/10.3826/jhr.2009.2944-I

Shiono, K., & Knight, D. (1991). Turbulent open channel flows with variable depth across the channel. *Journal of Fluid Mechanics*, *222*, 617–646.

Stocchino, A., & Brocchini, M. (2010). Horizontal mixing of quasi-uniform, straight, compound channel flows. *Journal of Fluid Mechanics*, *643*, 168–198. https://doi.org/10.1017/S0022112009992680

Terrier, B. (2010). Flow characteristics in straight compound channels with vegetation along the main channel (Ph.D. thesis), Loughborough University.

Tockner, K., & Stanford, J. (2002). Riverine floodplains: Present state and future trends. *Environmental Conservation*, *29*(03), 308–330. https://doi.org/10.1017/S037689290200022X

Uijttewaal, W., & Booji, R. (2000). Effects of shallowness on the development of free-surface mixing layersl. *Physics of Fluids*, *12*(2), 392–420.

Valentine, E. M., & Wood, I. R. (1979). Experiments in longitudinal dispersion with dead zones. *Journal of Hydraulic Division*, *105*(HY8), 999–1016.

van Prooijen, B., & Uijttewaal, W. (2002). A linear approach for the evolution of coherent structures in shallow mixing layers. *Physics and Fluids*, *14*(12), 4105–4114.

Van Rijn, L. (2007). Unified view of sediment transport by currents and waves. I: Initiation of motion, bed roughness, and bed-load transport,. *Journal of Hydraulic Engineering*, *133*(6), 649–667. https://doi.org/10.1061/(ASCE)0733-9429(2007)133:6(649)

Walling, D. E., & Owens, P. N. (1998). The role of channel and floodplain storage in the suspended sediment budget of the River Ouse, Yorkshire UK. *Geomorphology*, *22*, 225–242.

Weitbrecht, V., Kuhn, G., & Jirka, G. H. (2002). Large-scale PIV measurements at the surface of shallow water flows. *Flow Measurement and Instrumentation*, *13*(5), 237–245. https://doi.org/10.1016/S0955-5986(02)00059-6

Weitbrecht, V., Socolofsky, S. A., & Jirka, G. H. (2008). Experiments on mass exchange between groin fields and main stream rivers. *Journal of Hydraulic Engineering*, *134*(2), 173–183. https://doi.org/10.1061/(ASCE)0733-9429(2008)134:2(173)

White, B., & Nepf, H. (2009). Shear instability and coherent structures in shallow flow adjacent to a porous layer. *Journal of Fluid Mechanics*, *593*(1), 1–32. https://doi.org/10.1017/S0022112007008415

Yalin, M. S. (1985). On the determination of ripple geometry. *Journal of Hydraulic Engineering*, *111*(8), 1148–1155.

Yossef, M., & de Vriend, H. (2010). Sediment exchange between a river and its groyne fields: Mobile-bed experiment. *Journal of Hydraulic Engineering*, *136*, 610–625. https://doi.org/10.1061/(ASCE)HY.1943-7900.0000226